

Online Research @ Cardiff

This is an Open Access document downloaded from ORCA, Cardiff University's institutional repository: <https://orca.cardiff.ac.uk/id/eprint/142773/>

This is the author's version of a work that was submitted to / accepted for publication.

Citation for final published version:

Hawkins, Bryson A., Han, Jaeyeon, Du, Jonathan J., Lai, Felcia, Stanton, Stephen A., Divakarla, Shravan S., Groundwater, Paul W., Platts, James A. ORCID: <https://orcid.org/0000-0002-1008-6595> and Hibbs, David E. 2021. Analyzing hydration differences in cocrystal polymorphs: high-resolution X-ray investigation of caffeine-glutaric acid cocrystals. *Crystal Growth and Design* 21 (8) , pp. 4456-4467. 10.1021/acs.cgd.1c00358 file

Publishers page: <http://dx.doi.org/10.1021/acs.cgd.1c00358>
<<http://dx.doi.org/10.1021/acs.cgd.1c00358>>

Please note:

Changes made as a result of publishing processes such as copy-editing, formatting and page numbers may not be reflected in this version. For the definitive version of this publication, please refer to the published source. You are advised to consult the publisher's version if you wish to cite this paper.

This version is being made available in accordance with publisher policies.

See

<http://orca.cf.ac.uk/policies.html> for usage policies. Copyright and moral rights for publications made available in ORCA are retained by the copyright holders.



Analysing Hydration differences in Co-crystal Polymorphs: A High-Resolution X-Ray Investigation of Caffeine-Glutaric Acid Co-crystals

Bryson A. Hawkins,¹ Jaeyeon Han,¹ Jonathan J. Du,^{1,∞} Felcia Lai,¹ Stephen A. Stanton,¹ Shravan S. Divakarla,¹ Paul W. Groundwater,¹ James A. Platts,² and David E. Hibbs^{1*}

¹*Sydney School of Pharmacy, Faculty of Medicine and Health, The University of Sydney, NSW 2006 Australia*

²*School of Chemistry, Cardiff University, Cardiff, CF10 3AT, UK*

[∞] *Department of Biochemistry, Emory University, Atlanta, GA 30322, current address*

**Corresponding author: David E. Hibbs, david.hibbs@sydney.edu.au*

†Electronic supplementary information (ESI) available. CCDC 2074412 (Monoclinic Form I) & 2074413 (Triclinic Form II) . For ESI and crystallographic data in CIF or other electronic formats, see DOI: XXXXXXXX

ABSTRACT

Two polymorphic forms of caffeine (CAF)-glutaric acid (GLU) co-crystals have been studied *via* high-resolution X-Ray crystallography and Bader's Quantum Theory of Atoms in Molecules (QTAIM). For both the monoclinic, **(1)**, and triclinic, **(2)**, systems the experimental charge density distribution of the 1:1 ratio of CAF and GLU polymorphs have been determined and compared. Previous studies have determined that **(1)** is less stable than **(2)**, in relative humidity (RH) testing. Topological analysis of the electron density distribution (EDD) revealed little difference between the two polymorphs internal system. The packing densities (0.76 vs. 0.74) and lattice energies ($-101.1 \text{ kJ mol}^{-1}$ vs. $-107.1 \text{ kJ mol}^{-1}$) of **(1)** and **(2)**, respectively, are nearly equivocal, implying the differences of hygroscopicity between the two polymorphs is not due to crystal lattice porosity or stability. Analysis of the number and strength of hydrogen bonds for **(1)** and **(2)**, revealed 9 hydrogen bonds topologically in both polymorphs. The 'Classical' (O-H \cdots X) hydrogen bonds were similarly present in both polymorphs, stabilising the co-crystals. However, the sum of the stability produced from the 'non-classical' (C-H \cdots X) bonds is higher in **(2)**, $-27.6 \text{ kJ mol}^{-1}$ vs $-38.2 \text{ kJ mol}^{-1}$ for **(1)** and **(2)**, respectively. One of the 9 hydrogen bonds in **(1)** and **(2)** vary from each other, caused by the torsional rotation of the aliphatic carbon chain in GLU. This bond is critical for packing stabilisation, creating a parallelogram like packing arrangement in **(2)** compared to ribboning in **(1)**. Hirshfeld surface analysis found that the percentage of O-H \cdots X hydrogen bonds were near identical in **(1)** and **(2)**, (23.9% vs. 22.1%), however, the H \cdots H contacts were higher in **(2)** (61.4% vs. 65.8%, **(1)** and **(2)**, respectively) suggesting that more hydrogen based contacts require competitive displacement by water in the hydration of **(2)** compared to **(1)**. Additionally, a stabilising aromatic cycle stack between CAF molecules is present in **(2)** due to the varied parallelogram packing arrangement, which was absent in **(1)**; this provided

~11.3 kJ mol⁻¹ of stability to the system of (2). The solid-state entropy and molecular dipole moments (MDM) of (1) and (2) supported the relative stability of the individual polymorphs, with (1) having a higher entropy and dipole moment compared to (2), (123.2 J·K⁻¹·mol⁻¹ vs. 112.8 J·K⁻¹·mol⁻¹, and 7.45 D and 4.93 D, for (1) and (2), respectively) implying it has the potential to hydrate more rapidly. These findings are in good agreement with previous experimental RH stability studies, giving further insight into the information gained from thermally averaged ground state crystal electron density data.

■ INTRODUCTION

Polymorphism is the ability of a chemical compound to exist in two or more distinct crystal forms. Different polymorphs often display vastly different physicochemical properties, such as stability, solubility, and hygroscopicity. Comparing polymorphic crystal forms allows the investigation of identical chemical constituents' and the outcome on the structure/property relationship differences. Analysis and understanding of the physicochemical changes in pharmaceutical polymorphs is vital in drug development. The variations seen in drugs will significantly impact whether a drug reaches the market, where a common reason for failure is poor solubility/hygroscopic stability.¹ One growing field that addresses these stability issues is co-crystallisation, whereby a non-active co-former is crystallised with the Active Pharmaceutical Ingredient (API) in a defined stoichiometry. The poor physicochemical properties of the methylxanthine alkaloid, caffeine (CAF, Figure 1(a)) were addressed when co-crystallised with dicarboxylic acids.^{2,3} CAF is one of the most commonly used central nervous stimulants in the world.⁴ Aside from its consumption as a beverage, CAF is also used to treat migraines, headaches and bradycardia.⁴ CAF, like all methylxanthines, has poor solubility at room temperature (16 mg/ml at room temperature, 200 mg/ml at 80°C, or 666 mg/ml at 100°C), and poor stability in high humidity settings.^{2,3} Dicarboxylic acids have been used extensively as co-formers in co-crystal engineering to optimise these stability shortcomings.^{2,3,5,6} This is primarily due to the carboxylic acid moiety being

able to simultaneously act as hydrogen bond donors and acceptors, thus they can form intermolecular bonds with a wide range of chemical species. A series of CAF-dicarboxylic acid co-crystals have been studied by Trask *et al.*, which found co-crystallisation attenuates the hygroscopic nature of CAF in relative humidity (RH) testing.³ They identified two polymorphs of the caffeine-glutaric co-crystal (CAF-GLU); a monoclinic form (Form I) (**1**) and a triclinic form (Form II) (**2**).³ Both (**1**) and (**2**) have a notable difference in hygroscopicity, solubility, stability and packing ability.^{2, 3, 5, 6} This confirms that polymorphism in co-crystal systems alters physicochemical properties differently following previous findings of single-component crystal systems.^{7,8} Further, Thakuria *et al.* documented the hydration pathway for (**1**) and (**2**) *via* series of controlled humidity environments, finding that (**1**) rapidly converted to (**2**) within 24 hours before an extended hydration phase (two weeks) causes (**2**) to form CAF monohydrate.² Further, it was suggested that the conversion of (**1**) to (**2**) was caused by the lower number of hydrogen bonds present in (**1**) compared to (**2**).² As well as the carbonyl oxygen position on the exterior of the crystal face of (**2**) was the reason for the hydration of (**2**) to the monohydrate form.²

Previously, the scientific community and our group have examined the electron density distribution (EDD) in polymorphic crystals and co-crystals to rationalise the physicochemical changes shown between forms.⁷⁻¹⁷ Attributing the common observed variation in physicochemical behaviour to be a result of changes in the EDD caused by the variation of weak intermolecular bonds and electrostatics created around the molecule(s).^{7, 8, 10-17} To date, high-resolution X-Ray analysis has not been employed to explain the differences seen in (**1**) and (**2**), as such, a charge density analysis of both CAF-GLU polymorphs reported by Trask *et al.* was performed and analysed using Bader's Quantum theory of Atoms in Molecules (QTAIM).¹⁸ Using experimental high-resolution electron densities for (**1**) and (**2**) and accompanying theoretical electron density, the comparison of the EDD properties obtained may assist in understanding the causes of differing hydration stability in these polymorphic co-crystals.

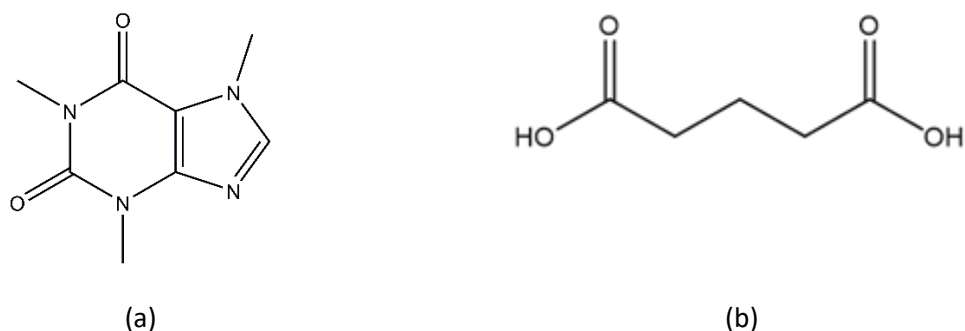


Figure 1. Chemical structures of (a) Caffeine (1,3,7-trimethylxanthine, CAF) and (b) Glutaric Acid (1,5-pentanedioic acid, GLU).

METHODS

CAF and GLU were purchased from Merck (Castle Hill, NSW, Australia) and used without further purification. Single Crystals of **(1)** and **(2)** suitable for diffraction were prepared *via* slow evaporation using the methods of Trask *et al.*³ A 1:1 molar equivalents of CAF and GLU were ground with 5 drops of chloroform for 90 mins.³ The resultant slurry was dissolved in chloroform, and single crystals suitable for X-Ray analysis were produced.³

The data for **(1)** and **(2)** were collected at The Sydney School of Pharmacy, Faculty of Medicine and Health, The University of Sydney, Australia using an Agilent Supernova™ X-Ray Diffractometer with a CCD Atlas detector at Mo \backslash K α wavelength (0.7107 Å), each specimen was cooled to 150 K throughout collection. The full details on data collection, integration, reduction, refinement, and data treatment for **(1)** and **(2)** can be found in the supporting information. The final multipole models (MM) selected for **(1)** and **(2)** were a combined TDS and an all-atom anisotropic displacement parameter model following the methods of Hawkins *et al.*, using all reflection data.⁹ The completeness of **(1)** and **(2)** were 99.67% and 99.77% respectively. The miller indices for missing reflections of **(1)** and **(2)** were removed in the data reduction process due bad profiles in sorting and averaging, these indices can be found in Supplementary Tables 18 and 19 .

Corresponding theoretical densities of **(1)** and **(2)** were generated from the high-order refinement coordinates from the MM, as the input geometry for gas-phase calculations for single-

point (SP) calculations only, the structures did not undergo geometry optimisation. The SP calculations were out using the Gaussian 09 suite at 6-31+G** level of theory.¹⁹ All calculations used the three-parameter hybrid exchange functional developed by Becke and the gradient corrected exchange-correlation potential by Lee *et al.* employed with the long-range correction parameter (CAM-B3LYP) proposed by Tawada *et al.*²⁰⁻²²

The topological analysis of the EDD was performed using the XDPROP module of XD for the experimental MMs, while the theoretical models were carried out using the AIMALL package.^{23,24}

Table 1. Selected crystallographic information for (1) and (2).

	(1)	(2)
Formula	C ₈ H ₁₀ N ₄ O ₂ · C ₅ H ₈ O ₄	C ₈ H ₁₀ N ₄ O ₂ · C ₅ H ₈ O ₄
Molecular Mass (g/mol)	326.30	326.30
Crystal size (mm)	0.2 x 0.2 x 0.15	0.3 x 0.2 x 0.2
Temperature (K)	149 (19)	150 (2)
Wavelength (Å)	0.71073	0.71073
Crystal system	Monoclinic	Triclinic
Space group	P2 ₁ /c	P $\bar{1}$
<i>a</i> (Å)	12.987 (2)	8.304 (2)
<i>b</i> (Å)	6.569 (2)	8.656 (10)

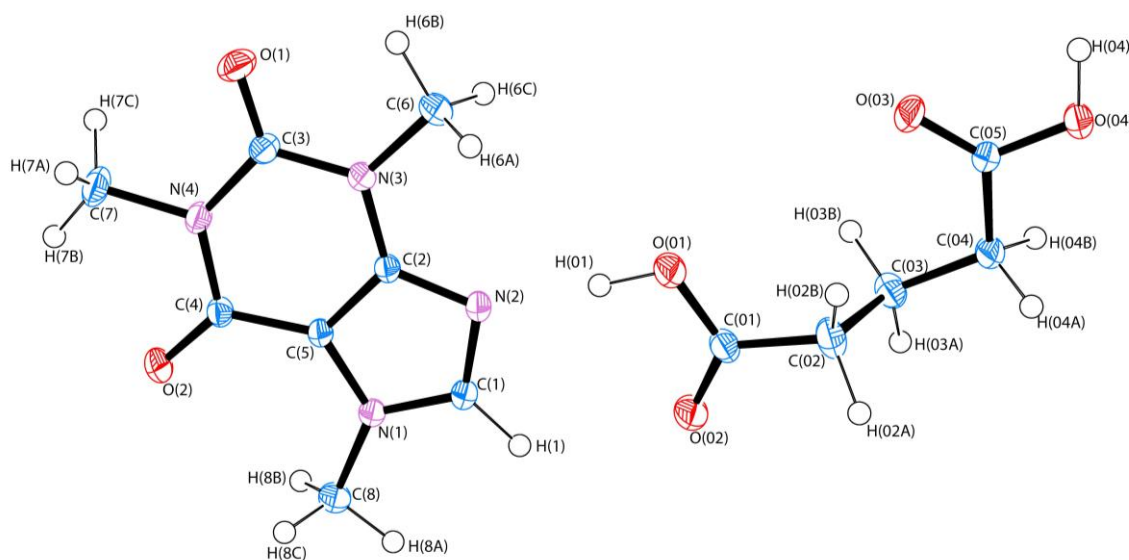
c (Å)	17.072 (3)	11.327 (3)
α (°)	90	68.85 (2)
β (°)	97.81 (2)	78.75 (2)
γ (°)	90	74.13 (2)
Volume (Å ³)	1443.25 (6)	726.47 (2)
Z	4	2
Refinement Method	Full-matrix least-squares on F^2	Full-matrix least-squares on F^2
No. of reflections	52814	50236
Collected		
No. unique	10124	11898
R_{int}	0.0420	0.0387
Completeness (%)	99.67	99.77
No. reflections used	10124	11891
ρ_c (g cm ⁻³)	1.502	1.492
$F(000)$	688.0	344.0
μ (mm ⁻¹)	0.11	0.12
$\sin \theta/\lambda_{\text{max}}$	0.9800	0.9995

Index ranges	$-24 \leq h \leq 24$	$-16 \leq h \leq 16$
	$-12 \leq k \leq 12$	$-17 \leq k \leq 15$
	$-32 \leq l \leq 32$	$-0 \leq l \leq 22$
IAM Refinement		
Final $R_{1\text{all}}, wR_{2\text{all}}$	0.066, 0.151	0.055, 0.160
Goodness of fit	1.13	1.05
Residual density ($e \text{ \AA}^{-3}$)	-0.329, 0.637	-0.490, 1.070
Multipole Refinement		
(TDS+SHADE)		
$N_{\text{obs}}/N_{\text{var}}$	15.475	16.077
$R(F), R(F^2), \text{all data}$	0.0654, 0.0464	0.0603, 0.760
$R(F), R(F^2) > 0\sigma(F)$	0.0515, 0.0459	0.0462, 0.0765
Goodness of fit (unscaled)	1.0866	1.6631
Residual density ($e \text{ \AA}^{-3}$)	-0.229, 0.201	-0.246, 0.375

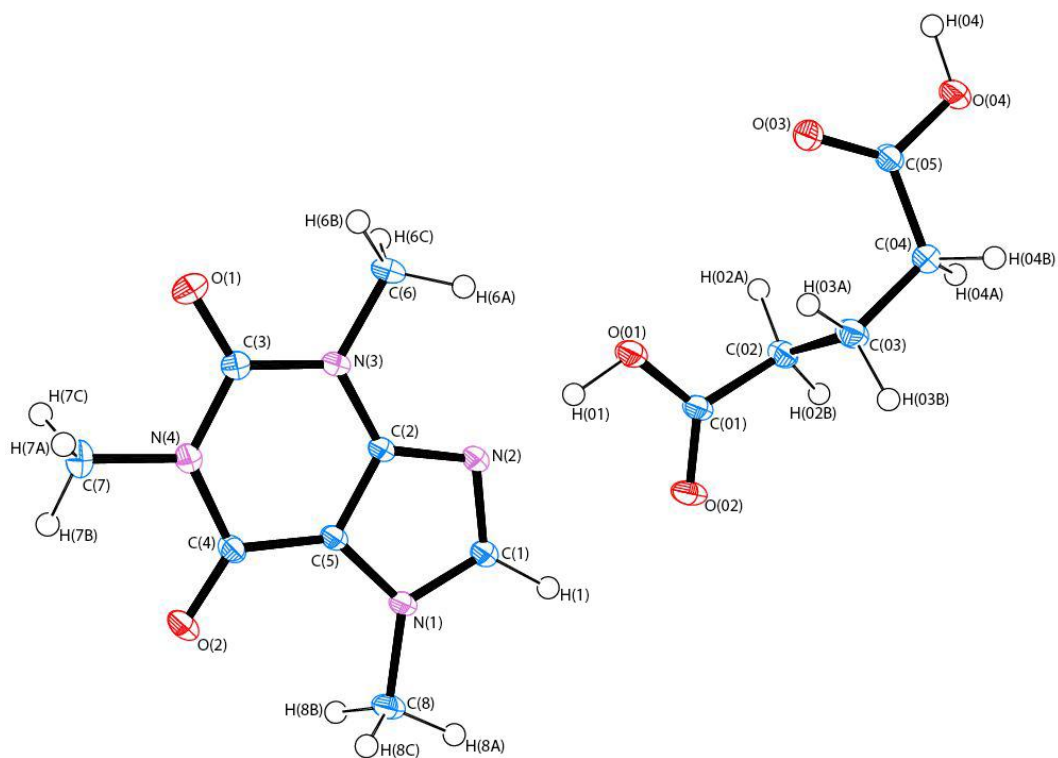
RESULTS AND DISCUSSION

Geometry.

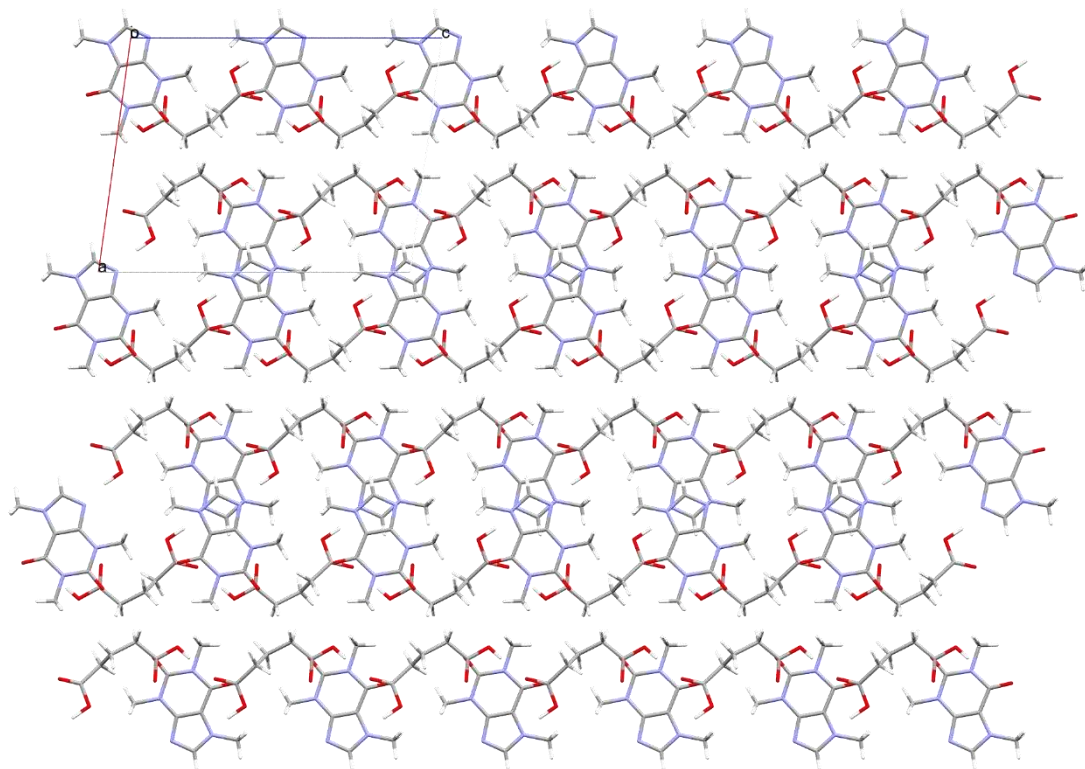
The resulting asymmetric unit structure can be seen in Figure 2 (a) and (b). The asymmetric units of (1) and (2) consist of a single CAF and GLU molecule. In both, the heterosynthon is seen between the imidazole group of CAF and carboxylic acid of GLU, comprising of two hydrogen bonds [O(01)-H(01) ... N(2), and C(1)-H(1) ... O(02)]. The aliphatic carbon chain in GLU is rotated in both (1) and (2) differently, the torsion angles are near identical but in opposite directions, 161.60° and -165.89° , respectively, [C(01)-C(02)-C(03)-C(04)]. The torsion angle change in GLU results in the packing variation between (1) and (2). Figure 2(c-d and e) shows the packing arrangement of (1) and (2), the b-axis in Figure (2 c and d) were selected for clarity. It is seen in (1) (Figure 2c) that packing is sheet-like, created by chaining of repeated CAF and GLU molecules parallel to one another. Conversely, in (2) (Figure 2d), the packing is antiparallel between the CAF and GLU. Additionally, the sheet alignment lays on a $\sim 45^\circ$ angle to the b-axis, creating a packing assembly like a parallelogram. There was a total of 9 hydrogen bonds geometrical identified for both (1) and (2), of which 7 were carbon donated hydrogen bonds from the carbocyclic acids, (C-H ... X). Leiserowitz commented on the role of C-H ... X bonds, noting that these bonds are critical for molecular alignment, and these will be discussed later.²⁵



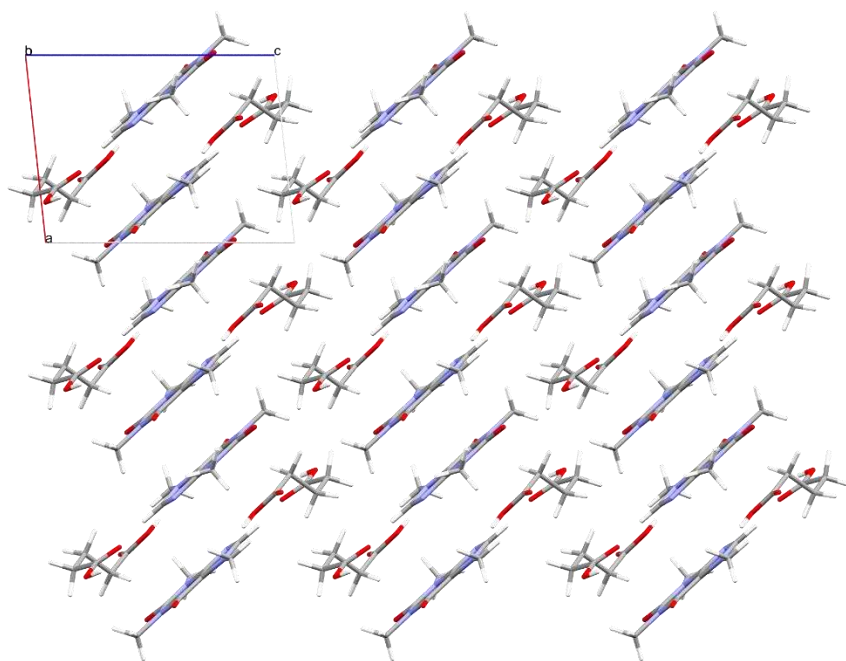
(a)



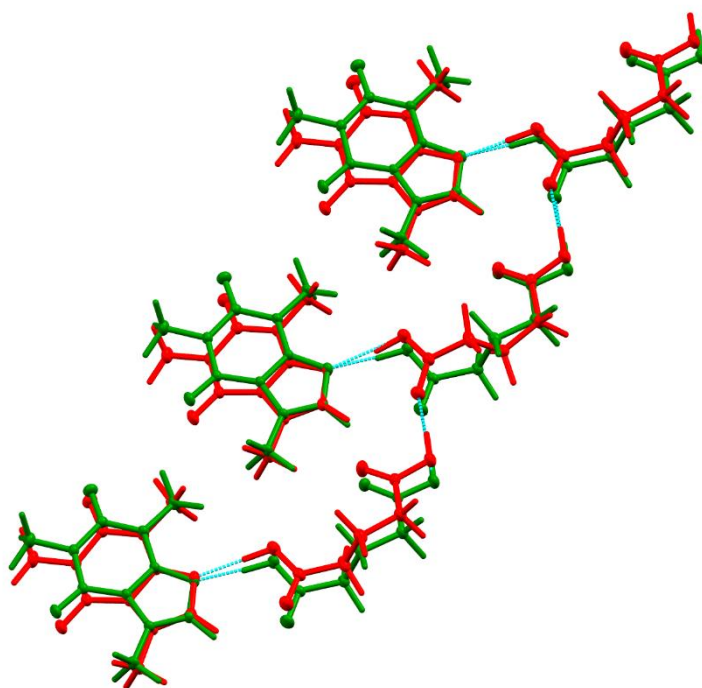
(b)



(c)



(d)



(e)

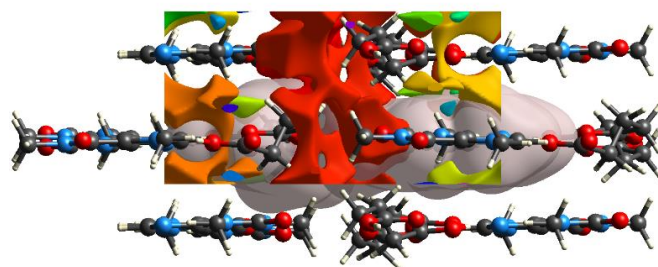
Figure 2. (a) ORTEP diagram of **(1)**, (b) ORTEP diagram of **(2)**, with generic labelling scheme used throughout. Thermal ellipsoids are at 50% probability. (c) 5 x 5 x 5 unit cell crystal packing of **(1)** along b-axis, and (d) 5 x 5 x 5 unit cell crystal packing of **(2)** along b-axis. (e) Molecular Overlay of **(1)**, (red) and **(2)**, green.^{26,27}

As stated, **(1)** is less stable than **(2)** when undergoing hydration resulting from humid conditions, with **(1)** transforming to **(2)** throughout the controlled humidity testing.³ A review of critical geometrical features, such as atomic packing factor (APF) and crystalline void space percentage, provides insight into the water aided dissociation vulnerability of each crystal lattice. The PLATON program was used to calculate the APFs and solvent accessible space (SAS) of **(1)** and **(2)**.²⁸ Neither **(1)** or **(2)** were found to have any SAS within their crystal lattices. However, the lattice of **(2)** was packed slightly less dense compared to **(1)**, 0.76 vs. 0.74, respectively, so this is unlikely to be the cause of instability to humidity.

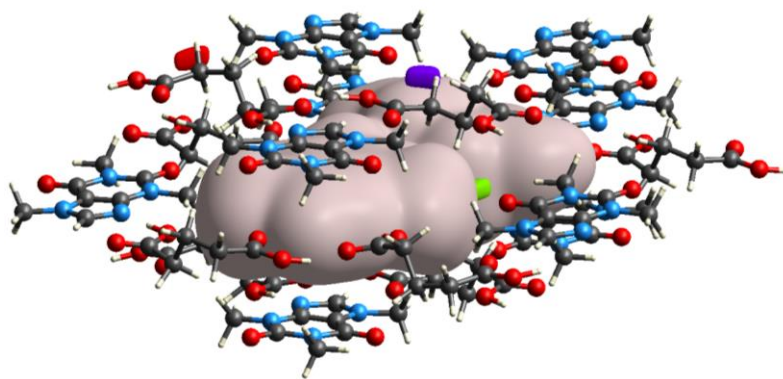
Another method to review the geometrical stability of packing is to examine the potential SAS space seen in the crystal when using the promolecule density. This is achieved by generating a Hirshfeld surface of the CAF-GLU molecules; then, a further surface is generated to map the void space, which can then be used to indicate the crystal lattice porosity. The functional or static porosity of a crystal is obtained by changing the isovalue in the calculation, a key parameter defined by Turner *et al.*²⁹ Turner *et al.* noted non-porous crystals require an isovalues of 0.002 au to find the potentially accessible void; however, a further calculation at 0.0005 au identify any permeant void in the crystalline lattices.²⁹ Like the APF calculations, the results were near equivocal; however, the void volume to total volume percentage (VV%) showed that **(1)** was slightly less porous than **(2)**. These voids are represented in Figure 3. The voids can be seen casing the asymmetric unit (voids=coloured, the variation of colour allow for the breakdown of the VV% in the contribution area, promolecule electron density/asymmetric unit=grey). Visually the voids are equally sized at both isovalues

indicating the SAS and permanent voids in **(1)** and **(2)** are equivalent (VV% of 6.11% and 0.16% for **(1)** and 6.70% and 0.25% for **(2)** at 0.002 and 0.0005 au, respectively). Interestingly, in figure 3(b), a permanent void is nested outside the asymmetric unit **(1)** at 0.0005 au. This feature is not present in **(2)** and indicates the gross solvent exposure if the lattice surface should be less. This suggests that upon water approaching the crystal lattice of **(1)** it has the potential to interact faster with the lattice surface, disrupting the lattice integrity and propelling polymorphic transformation to form **(2)**. Although, overall, the geometrical analysis, SAS and VV% indicate that the geometrical stability of the two crystals to be similar. This corresponds with Berkovitch-Yellin *et al.*, noting that conformational change in two packing arrangements of α -glycine showed the bond energies maintaining the packing planes to be very similar (-13 and -9 kJ mol⁻¹).³⁰

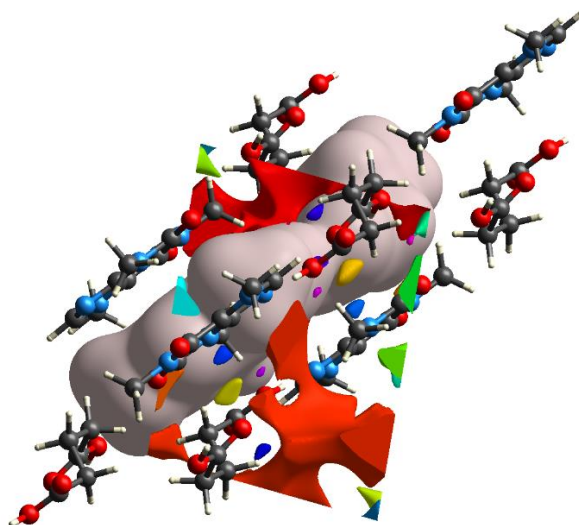
The above suggests that the polymorphic transition of **(1)** to **(2)** caused by water probing the lattice of **(1)** has to be energetically favourable, then the subsequent assembled lattice of **(2)** must be deconstructed incrementally throughout hydrate formation. This is very likely the result of EDD changes in **(1)** and **(2)** and how the incoming water molecules potentially interact with the various weak bonds present, which will be explored below.



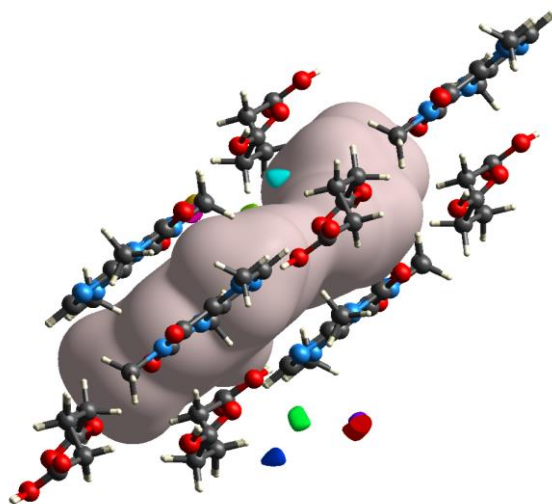
(a)



(b)



(c)



(d)

Figure 3. (a-b) Void spaces depicted in colour domains for **(1)** at 0.002 au and 0.0005 au, respectively. (c-d) Void spaces depicted in colour domains for **(2)** at 0.002 au and 0.0005 au.³¹

Topological Analysis.

Topological analysis of **(1)** and **(2)** were carried out using Bader's QTAIM, with the completeness of both investigations substantiated by the satisfaction of the Poincaré-Hopf relationship for the theoretical models or its crystalline equivalent Morse relationship in the experimental MM of **(1)** and **(2)**.³² Good agreement was found between the SP and MM models for both **(1)** and **(2)**. With the experimental model varying from the SP models by an average of ρ_{bcpr} and $\nabla^2\rho_{\text{bcpr}}$ of $0.135 \text{ e } \text{\AA}^{-3}$ and $-2.58 \text{ e } \text{\AA}^{-5}$, and, ρ_{bcpr} by $-0.053 \text{ e } \text{\AA}^{-3}$ and $\nabla^2\rho_{\text{bcpr}}$ by $0.67 \text{ e } \text{\AA}^{-5}$, for **(1)** and **(2)** respectively. The most significant variations from the SP models were seen around $\nabla^2\rho_{\text{bcpr}}$ of carbonyl oxygen environments, and this can be attributed to the lack of a crystal field effects in the gas phase SP models and experimental $\nabla^2\rho_{\text{bcpr}}$ often is more enhanced in areas of charge change, as **(1)** is a metastable intermediate of **(2)** the large differences in the $\nabla^2\rho_{\text{bcpr}}$ could be attributed to the repositioning of the EDD in the formation of **(2)**.

The topological analysis of **(1)** and **(2)** revealed little difference in each molecule's intramolecular EDD but highlighted some other differences in the intermolecular EDD, discussed below.

As mentioned previously, the importance of saturated carbon chains, creating non-linear packing arrangements, can profoundly affect the packing geometry.³³ As seen in Figure 2(d), the GLU molecule rotation results in staggering of the lattice creating a more perpendicular sheet of CAF and GLU molecules in the lattice assembly of **(2)**. This sheeting results in the formation of an aromatic cycle stacking between the CAF moieties. This interaction was created by the symmetrical C(1)-C(2) ... C(1)-C(2) bonding motif, $\rho_{\text{ring}} 0.031 \text{ e } \text{\AA}^{-3}$, and $\nabla^2\rho_{\text{ring}} 0.3 \text{ e } \text{\AA}^{-5}$. Validated energies for aromatic cycle stacking systems were previously published by Waller *et al.*, as this system contains two ρ_{bcpr}

making up a four-membered ρ_{ring} this system is estimated to stabilise **(2)** by $\sim 11.3 \text{ kJ mol}^{-1}$.³⁴ No aromatic cycle system was identified for **(1)** suggesting that the inversion of the torsion angle in GLU creates a parallel sheet packing environment, causing the CAF moieties to not overlap.

Furthermore, the aromatic cycle stacking within **(2)** creates a hydrophobic residential region within the crystal lattice. It can be postulated that the adhesion of water to the lattice would be lower due to the repulsion effects. Thakuria *et al.* have previously reported that **(1)** is converted to **(2)** within 24 hours before forming CAF monohydrate over a period of weeks in RH testing.³ This suggests the possibility of the rapid conversion of **(1)** to **(2)** is due to an attack by water molecules disrupting the bonds maintaining the torsional geometry of GLU in the crystal lattice of **(1)**. This will be reviewed further below in hydrogen bond topology. Refer to ESI for the full topological analysis tables.

Hydrogen Bond Topological Analysis.

Thakuria *et al.* found that there were 2 more hydrogen bonds present in **(2)** compared to **(1)** (9 vs. 7, respectively). These extra bonds were presumed the cause for increased stability, as observed in the hydration study.² However, for both systems **(1)** and **(2)**, 9 hydrogen bonds were identified topologically, suggesting that the relative stabilities should be nearly equal. A simple method to assess this concept of enhanced stability is by utilising the 'UNI' force field intermolecular potential method Gavezzotti *et al.*³⁵ This method offers a stability prediction based on an empirical intermolecular potential value of the weak bonds within a 15 molecule cluster. This method agreed with Thakuria *et al.* with the hydrogen bond systems in **(1)** and **(2)** having a total intermolecular bonding stability of -239.4 and $-241.7 \text{ kJ mol}^{-1}$ for **(1)** and **(2)**, respectively.² However, the minimal difference in intermolecular energies aligns well with the equal number of hydrogen bonds found in each polymorph, similarly coinciding with the stability work of Turner *et al.*, which found conformational polymorphs of oxalic acid clusters had calculated stability energies within standard error.³⁶ The above stability findings highlight that clusters of conformational polymorphs require an

individual appraisal of the bond networks. This is usually performed by topological analysis of hydrogen bonds allowing for each bond to be independently judged, critiquing the importance in the lattice and providing bond strengths for the bonds maintaining the lattice. As such, the topological analysis of the weak bonds present may allow validation of Thakuria *et al.* proposition and offer insight into increased observed stability of **(2)**.²

Topological review of the hydrogen bonding environments in small molecules is an area of focus in charge density analysis, more so particularly on data from experimental EDDs. Many criteria have been proposed for analysis of BCP to denote whether they are a hydrogen bond, for example Espinosa *et al.*, whom found that the positive λ_3 curvature at the BCP is the most meaningful parameter in defining the BCP as a hydrogen bond.³⁷ Moreover, the work of Koch *et al.* and Wood *et al.* were utilised to categorise the hydrogen bonds present in both **(1)** and **(2)**.^{38,40} Koch *et al.* defined hydrogen bond types, defining categories of 'classical' and 'non-classical' hydrogen bonds, whereby oxygen or nitrogen donated hydrogens (O-H \cdots X or N-H \cdots X) are considered 'classical' and carbon donated hydrogen bonds (C-H \cdots X) are considered 'non-classical' in silico.³⁸ Many experimental charge density studies have been performed in support of the proposal of Koch *et al.*, such as Ranganathan *et al.*, who probed the EDD of various crystals with differing hydrogen bonding environments, where their results obtained were in agreement with the prior work on the definitions of hydrogen bond groupings.³⁹ Wood *et al.* drew the connection between the Donor – Hydrogen – Acceptor - Angle (DHA $^\circ$) directionality and bond interaction energy, finding linear DHA $^\circ$ s resulted in stronger interactions.⁴⁰ Further to this, the topologically identified hydrogen bonds had hydrogen bond strengths calculated using the methods developed by Abramov and Espinosa, and then categorised by strength based on the work by Hibbert *et al.*; hydrogen bonds as weak ($E_{\text{HB}} < 20$ kJ mol $^{-1}$), moderate ($E_{\text{HB}} = 20\text{-}40$ kJ mol $^{-1}$) and strong ($E_{\text{HB}} > 60$ kJ mol $^{-1}$).⁴¹⁻⁴⁴

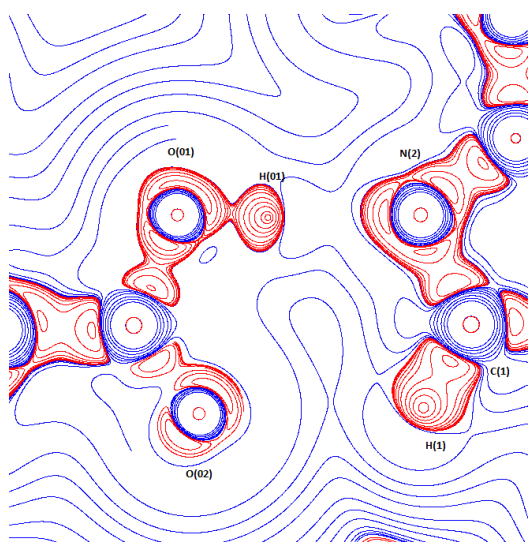
As mentioned above, there are 9 hydrogen bonds present in both **(1)** and **(2)**. Trask *et al.* and Thakuria *et al.* noted the formation of a heterosynthon based interaction between the imidazole of

CAF and the carboxylic acid of GLU.^{2,3} The heterogenous synthon is formed between one 'classical' and 'non-classical' hydrogen bond O(01)-H(01) \cdots N(2) and C(1)-H(1) \cdots O(02), respectively. The synthon strength in (1) compared to (2) is stronger overall, with the O(01)-H(01) \cdots N(2) bond being -48.7 and -44.6 kJ mol⁻¹, and the C(1)-H(1) \cdots O(02) bond being -6.7 and -6.0 kJ mol⁻¹, respectively. The nitrogenous donated bond strengths can be explained by Nguyen *et al.*, whereby the donor hydrogen atom to lone pair electrons (LPs) angle, (DH-LP^o), influenced the resultant strength of hydrogen bond interactions.⁴⁵ This concept of Nguyen *et al.* was seen in the experimental charge density study of Schmidtamm *et al.*, where a similar hydrogen bonding environment was seen in the polymorphic isonicotinamide-oxalic acid co-crystals, with nitrogen acceptor atom producing a stronger hydrogen bond strength.^{12, 45} The DH-LP^o of the nitrogen-based bond are shown in the contour map below (Figure 3). The more direct relationship of DHA^o and DH-LP^o is seen in (2) 178.10^o vs. 176.10^o and (1) 172.93^o vs. 169.65^o, respectively. For the C(1)-H(1) \cdots O(02) portion of the heterogenous synthon, the bond meets Munshi *et al.* experimental work on separation of the hydrogen bond and van der Waals like interactions overlap for C-H \cdots O bonding.^{46,47} The bonds are within the defined bond range for both (1) and (2), being 2.53 Å in length for both crystals, with the acceptor having a larger distance to the BCP, with near identical $d_{H\cdots bcp}$ and $d_{A\cdots bcp}$ (Tables 2 and 3). This highlights the importance of C-H \cdots X interactions in synthon formation and stabilisation, planar nature of the terminal groups of GLU alongside the imidazole region of CAF create a flat synthon environment resulting in the near identical hydrogen bond strengths. However, the synthon as whole in (1) and (2) calculated hydrogen bonds strengths using the Abramov and Espinosa methods fall within experimental error and are unsurprising due identical terminal portions of GLU in (1) and (2).⁴¹⁻⁴³ Yet, the carbon donated bond that completes the heterogynous synthon is 'non-classical' and weak following the classifications of Koch *et al.* and Hibbert *et al.*^{38,44} The LPs of O(02) for (2) are polarised away from the synthon towards the intermolecular bond with O(04)-H(04), this bond is 'classical', and the DH-LP^o aligns more to the DHA^o (168.2 vs. 167.9^o, respectively), a greater electron density (ρ_{bcp}) (0.1 e Å⁻³) is calculated. As a result, it has a moderate hydrogen bond strength (-26.7 kJ

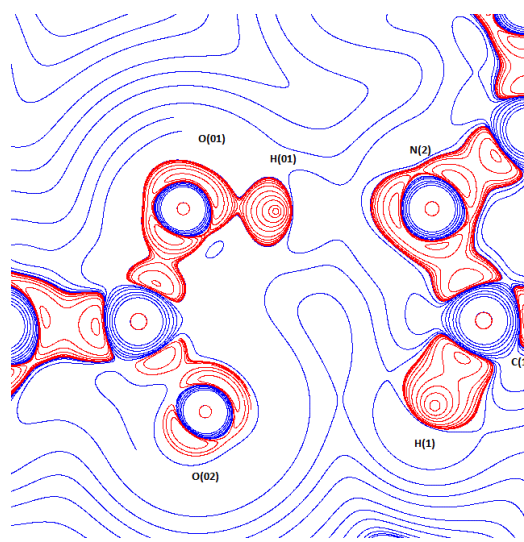
mol⁻¹). Similarly, this bond is found in **(1)** as expected due to the torsion angle, not affecting the terminal carboxylic portions on GLU, this bond is moderately strong (-30.8 kJ mol⁻¹). This suggests that the heterogenous synthon is not the site for observed differences seen in **(1)** and **(2)** stability.

The remaining topological bonds found in both systems are all 'non-classical'. They inherently are all weak and all meet the defining details of Munshi *et al.*^{38,39,40,46} Together, however, the bonds collectively offer substantial stabilisation energy, and the summation of these bonds corresponds with the expected observed outcome of **(1)** being less stable than **(2)**. These bonds have a summed total is -31.45 and -38.22 kJ mol⁻¹ for **(1)** and **(2)**, respectively. This suggests that the required energy to disrupt the aliphatic carbon donated bonds in the lattice is lower in **(1)**. The only non-communal hydrogen bonds present in both **(1)** and **(2)** is C(6)-H(6B)⋯ O(2) and C(04)-H(04B) ⋯ O(1), respectively. This bond difference is caused by the rotation of the aliphatic GLU chain, and these bonds are weak, fitting the above archotyping. Interestingly, the C(04)-H(04B) ⋯ O(1) of **(2)** is -2.61 kJ mol⁻¹ stronger than that of the C(6)-H(6B)⋯ O(2), this can be attributed to the DHA° of each interaction. In C(6)-H(6B)⋯ O(2) in **(1)** has a considerable variation between the DHA° and the DH-LP° 121.01° vs. 107.88°, respectively. Compared to that of C(04)-H(04B) ⋯ O(1) in **(2)** being 128.13° vs. 120.22°, for the DHA° and DH-LP°, respectively. Based on the known rotational of the aliphatic carbon chain within GLU, it can be stipulated that this observed difference creates a better stabilisation of the lattice due to the near non-existent difference of any other hydrogen bond **(1)** and **(2)**. Previously, Nguyen *et al.* discussed the conformational energies of GLU polymorphs alone, finding that the C_{2v} *cis* conformer II is predicted to be the most stable of the various polymorphs in the gas phase.⁴⁷ This alongside the observable rotation suggests it may influence the stability within a co-crystal system. The rotation of the aliphatic carbon chain with C(03) being the pivot of torsion, results in C(03) to face away from the pyrimidine (Figure 2(b)) in **(2)**. Leiserowitz discussed the direction of aliphatic carbon bonds having considerable importance in packing variation as mentioned above; however, here, it can be seen that the GLU moiety taking the crystallised conformation creates the environment for the C(04)-H(04B) ⋯ O(1) bond seen in **(2)** and resultantly

creates branching of the lattice creating CAF overlap resulting in the aromatic cyclic stack. Alongside the more direct angle of the bond formation and shorter $d_{H\cdots bcp}$ and $d_{A\cdots bcp}$ gives more dexterity to the packing in **(2)**.^{25,47} Due to the planar groups in both crystals perpendicular interactions occur, stemming from the above mentioned interactions and the C-H donated hydrogen bonds. These as mentioned above are from predominately identical donor atoms in both **(1)** and **(2)**, all of these bonds have similar contributing strengths to the packing lattice as shown tables 2 and 3, with given exception being the C-H bond formed by the torsional rotation around C(03) suggesting it torsional position in **(2)** is preferred energetically. The hydrogen bonds identified in the topological analysis and the contributor strength for each bond can be found in Tables 2 and 3.



(a)



(b)

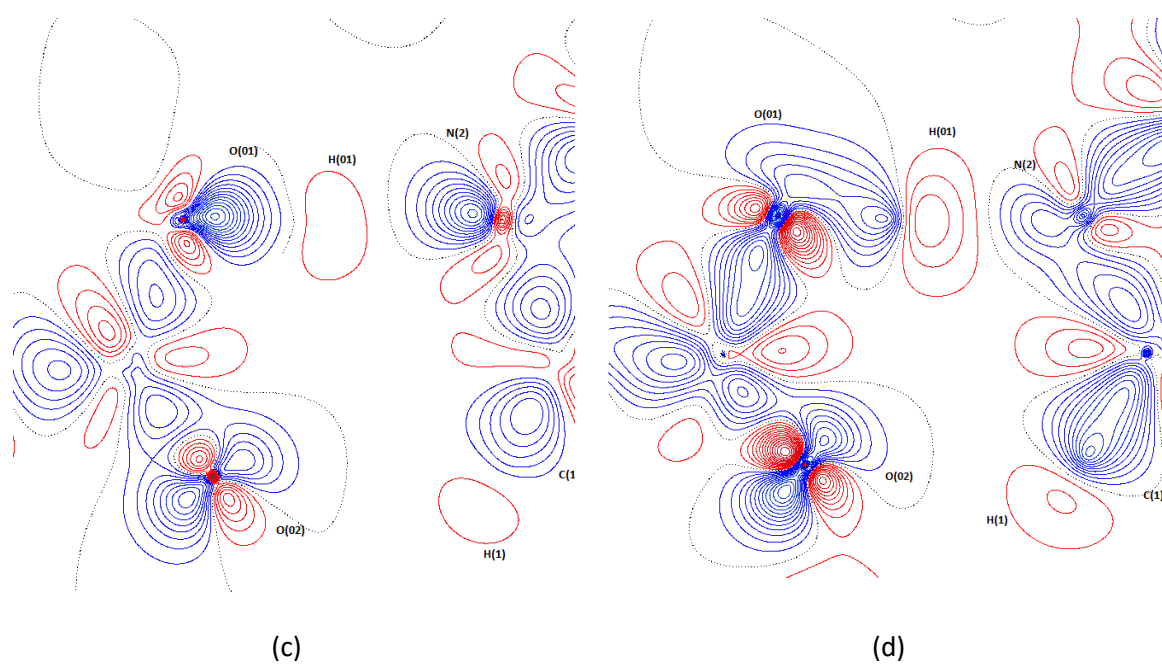


Figure 4. Laplacian ($-\nabla^2\rho$) contour diagrams and static deformation density plots of the heterosynthon in **(1)**, (a), (c) and **(2)**, (b), (d), respectively. All represented in the N(2)-O(01)-O(02) plane.³³

Table 2. Topological analysis of hydrogen bonding in **(1)**.

Bond	ρ ($e \text{ \AA}^{-3}$)	$\nabla^2\rho$ ($e \text{ \AA}^{-5}$)	ϵ	$d_{\text{H}\cdots\text{bcp}}$ (\AA)	$d_{\text{A}\cdots\text{bcp}}$ (\AA)	E_{HB} (kJ mol^{-1})
Interactions within the asymmetric unit						
O(01)-H(01)⋯ N(2)	0.24(002)	4.51(001)	0.06	0.57	1.17	-48.66
C(1)-H(1) ⋯ O(02)	0.06 (022)	0.80(027)	0.08	1.08	1.45	-6.72

Interactions
outside the
asymmetric
unit

C(8)-H(8A) ... O(03) ^c	0.05 (004)	0.96 (002)	0.17	1.18	1.51	-6.60
C(1)-H(1) ... O(03) ^c	0.07 (008)	1.16 (002)	0.19	0.86	1.37	-9.69
C(7)-H(7B) ... O(04) ^c	0.05 (001)	0.65 (001)	0.41	1.18	1.51	-5.06
C(6)-H(6B) ... O(2) ^c	0.04 (002)	0.57 (001)	0.076	1.18	1.51	-4.16
O(04)-H(04) ... O(02) ^d	0.11 (023)	4.96 (031)	0.03	0.53	1.17	-30.88
C(8)-H(8C) ... O(01) ^b	0.03 (004)	0.49 (002)	0.03	1.11	1.56	-3.22
C(7)-H(7A) ... O(04) ^a	0.029 (002)	0.41 (001)	0.41	1.18	1.58	-2.72

^a -x+1, y+1/2, -z +1/2, z-1/2; ^b x, -y+3/2, z+1/2; ^c x, -y+3/2, z-1/2; ^d x, -y+3/2, z-1/2; ^e

Table 3. Topological analysis of hydrogen bonding in (**2**).

Bond	ρ (e Å ⁻³)	$\nabla^2\rho$ (e Å ⁻⁵)	ϵ	$d_{H\cdots bcp}$ (Å)	$d_{A\cdots bcp}$ (Å)	E_{HB} (kJ mol ⁻¹)
Interactions within the asymmetric unit						
C(1)-H(1) ... O(02)	0.06 (002)	0.76 (001)	0.35	1.07	1.46	-6.00
O(01)-H(01) ... N(2)	0.18 (041)	5.97 (057)	0.12	0.52	1.18	-44.56
Interactions outside the asymmetric unit						
C(1)-H(1) ... O(03) ^a	0.09 (009)	1.47 (001)	0.23	1.21	0.86	-12.10
C(8)-H(8A) ... O(03) ^b	0.06 (009)	0.91 (002)	0.11	0.99	1.45	-6.67
C(7)-H(7B) ... O(04) ^c	0.05 (003)	0.71 (001)	1.64	1.14	1.45	-4.99
C(7)-H(7C) ... O(04) ^d	0.02 (002)	0.33 (001)	0.55	1.30	1.59	-2.12
C(8)-H(8C) ... O(2) ^e	0.05 (013)	0.84 (001)	0.08	0.95	1.43	-5.57

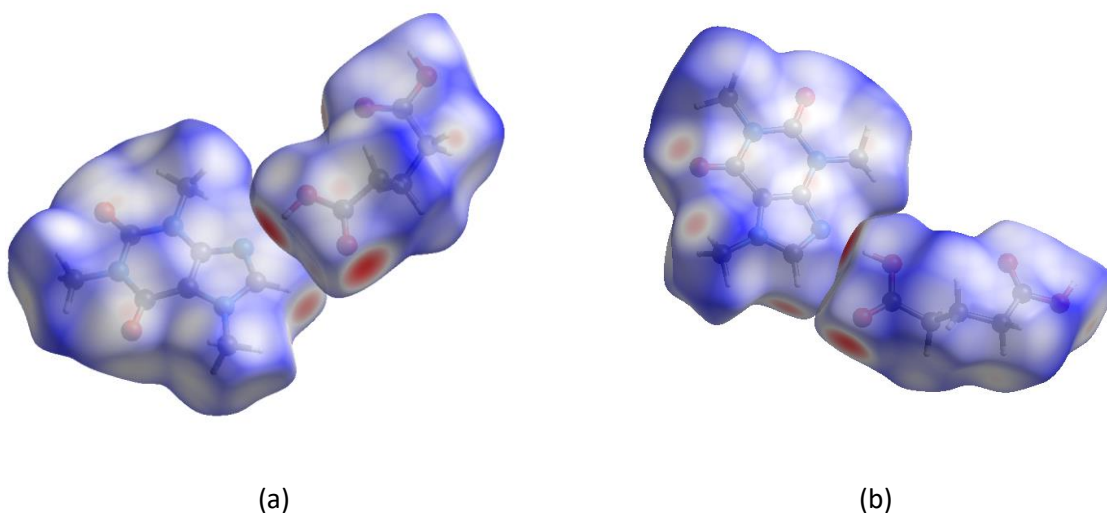
C(04)-H(04B) ...	0.06 (002)	0.81 (001)	0.22	1.11	1.44	-6.77
O(1) ^f						
O(04)-H(04) ...	0.10 (027)	4.32 (022)	0.27	0.57	1.19	-26.70
O(02) ^g						

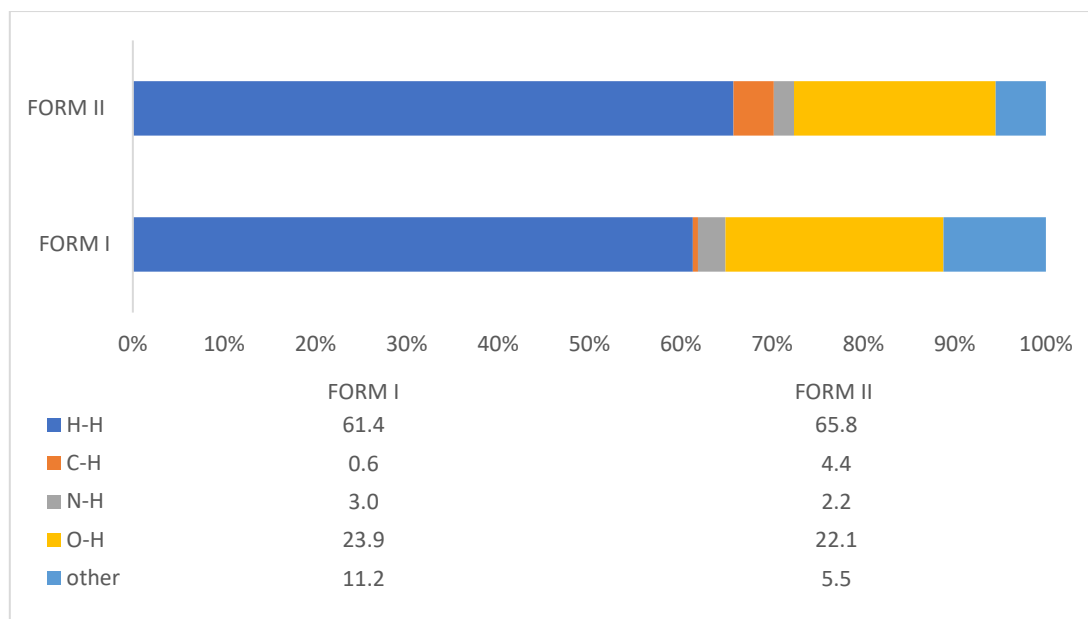
^ax,y+1,z; ^b-x,y-2,z-1; ^cx-1,y+1,z+1; ^d-x+1,-y, -z+1; ^e-x,-y+2, -z+1; ^fx+1,y,z-1; ^gx,y-1,z

Hirshfeld Analysis.

A 3-Dimensional surface representation of the promolecule density equal to 50% of the total crystal density is referred to as a Hirshfeld surface. Hirshfeld surface diagrams are visual depictions of the d_{norm} surfaces, which are the sum of normalised van der Waals radii (d_e & d_i) of atoms involved in an interaction. These van der Waals radii measure the distance from the nucleus to the surface of an atom (d_i) and from that surface to a neighbouring atom's nucleus (d_e). The colours of the surface relate to the proximity of the atoms involved. Red areas identify contacts closer than the sum of their van der Waals radii. In contrast, blue regions of the surface depict distances longer than the sum of their van der Waals radii and white show contacts equal to the sum of the van der Waals radii. The Hirshfeld surface and associated fingerprint plots of both **(1)** and **(2)** were generated using the CrystalExplorer program, and the surfaces can be seen in Figure 5.³¹ The key intermolecular bonds are clearly shown in both the **(1)** and **(2)** surfaces, the strong red region around the imidazole moiety highlights the heterosynthon created between CAF and GLU. Further to this, the intermolecular bonds within and extending from the asymmetric unit can be seen across the surfaces. As **(1)** and **(2)** are polymorphs, understanding which atoms contribute to weak interactions may offer insights into their physically observed differences. Adjustment for the potential theoretical random contacts formed across the Hirshfeld surfaces were addressed by calculation of the

enrichment ratio (E), found by the expression $E = \frac{C_{XX/XY}}{R_{XX/XY}}$, where X,Y are chemical species, C is the actual contribution to the surface by atom pairs (X-X or X-Y), and R is the potential random contacts between atoms, R can be calculated by probability products using summation of all contacts for a chemical species ($S_{X,Y}$) using the steps described by Jelsch *et al.*⁴⁸ The corrected contributions are represented in Figure 5, with the contributions of most elements to weak bonding being very similar between **(1)** and **(2)**. A significant difference is seen in the C-H group, where there are 3.8% more interactions **(2)**, which are located in the aromatic cycle stacking region. As both crystals have an identical chemical composition, it can be suggested that the involvement of the C-H group in **(2)** forming the cyclic stack, maintains the lattice integrity, and creates a deterrent for incoming water prior to hydration of the crystal. Furthermore, H-H contacts are higher in **(2)** suggesting a larger level of displacement of the van der Waals forces is required to hydrate the lattice of **(2)**. This follows the physically observed trend, whereby the decreased van der Waals forces and lack of aromatic cycle stack in **(1)** causes the rapid transformation to **(2)**, then a lengthy deliquescence of **(2)** to CAF and GLU before monohydrate formation.²





(c)

Figure 5. (a) Hirshfeld surface of **(1)**, (b) Hirshfeld surface of **(2)** and (c) graphical representation of the relative bond contribution % of the Hirshfeld surfaces.³¹

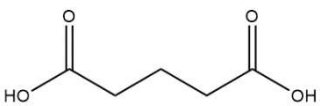
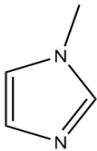
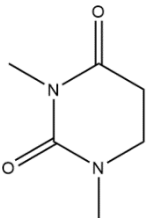
Atomic Charges and Electrostatics.

Bader charges (Ω) obtained from integration across the atomic basins bound by zero flux surfaces of the SP and MM of **(1)** and **(2)** were analysed. The charge of each atom in both polymorphs were minimally different. Du *et al.* previously showed how portioning atomic charge into separate molecular regions aided in the analysis of delocalisation/transfer of charge in co-crystals.⁴⁹ As such, the co-crystal was partitioned into 3 groups and summed these results can be found in Table 4. It showed that the dicarboxylic acid, the imidazole and pyrimidine moieties partitioned charges in **(1)** differ significantly from **(2)**, where the dicarboxylic acid in **(2)** is more negative compared to **(1)**.

In contrast, the CAF in **(2)** is significantly more positive, possibly due to charge transfer between the molecules. Similarly, the overall sum of parts shows **(1)** is more electronegative than **(2)**, mostly in the pyrimidine fragment. This could be due to the variation in the carbonyl bonds present within the pyrimidine for **(1)** and **(2)**, with C(04)-H(04B) \cdots O(1) present in **(2)** alone. The total sum shows that

there is a -0.35 e difference in total Bader charge in (1) compared to (2) suggesting to be more reactive when under the presence of water molecules. Furthermore, the fragment-based charges were then combined with the Bravais, Friedel, Donnay and Harker (BFDH) crystal morphology predictions generated within Mercury; these BFDH figures can be found in ESI.²⁷ In (1), the external BFDH crystal plane showed unimpeded access to the CAF moieties and half of the GLU chain, suggesting that the water can interact with the crystal surface and, consequently, outcompete the weak bonds on the crystal surface. Similarly, in (2) the BFDH morphology is predominantly found to have carbonyl oxygens across the crystal surface. Still, as these atoms are more occupied in intermolecular bonds, it suggests that outcompeting of the lattice's weak interactions occurs over a more extended period before hydrate formation happens in agreement with experimental findings.

Table 4. Partitioned Bader Atomic Charges of (1) and (2).

Ω (e)				Total
Σ (1)	-0.04	0.21	-0.66	-0.49
Σ (2)	-0.12	0.23	0.03	0.14

When the electrostatic potential (ESP) of a molecule is mapped upon the isosurface of the electron density (Figure 6), it allows visualisation of how atomic charge is distributed across a molecular system. Here, electronegative atoms are coloured red, while electropositive atoms are coloured blue, and this information can aid in visualising bond formation. Figure 6(a) illustrates the ESP surface of (1), it confirms the hydrogen bond donor behaviour of the GLU carbonyl oxygen, with the O(01)-H(01)⋯N(2) bond of the heterosynthon with the blue surface encapsulating N(2). Figure 6(b) is

the experimental ESP surface of **(2)**. Similarly, the carbonyl oxygens are red, showing the ability to form hydrogen bonds corresponding to the topology noted above. Both figures complement the graphic representation of fingerprint plots presented above, showing the importance of the oxygen atoms in each system in the formation of hydrogen bonds. The torsion angle change in GLU clearly shows the carbonyl oxygens' direction in both ESP figures, with **(2)** having bidirectionality allowing for the packing arrangements mentioned early, wherein **(1)** the GLU carbonyl oxygens are more lateral, causing the stringing packing arrangement. The complete list of atomic basin integration charges can be found in ESI.

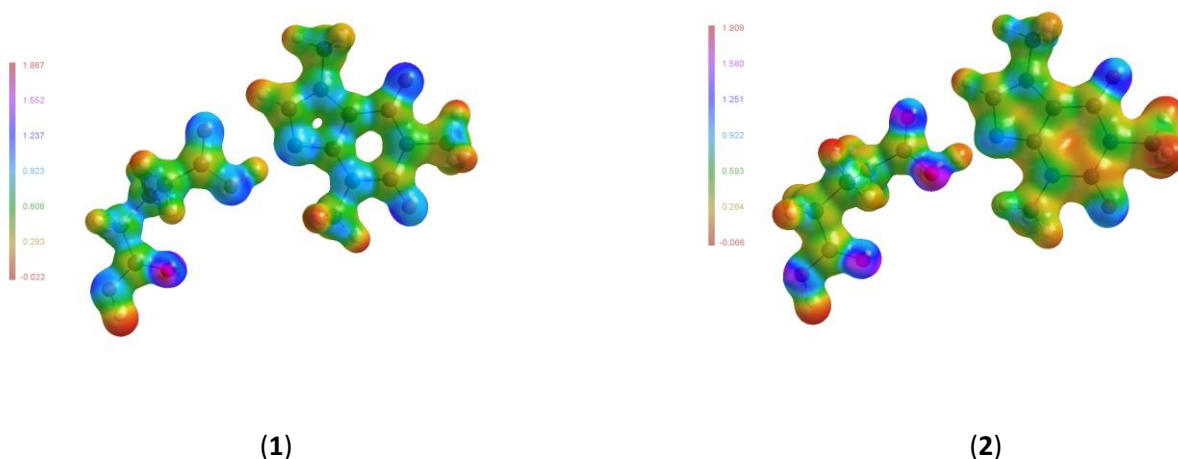


Figure 6. Molecular electrostatic potential (eV) maps of **(1)** and **(2)** mapped on an isosurface of ρ .⁵⁰

Lattice Energies and Stability.

Lattice energies give an insight into the solubility and stability of a crystalline substance. Lattice energies reflect the amount of energy required to deconstruct the lattice to liberate free molecules. As described above, **(1)** is the starting point of the polymorphic trend, undergoing a polymorphic transformation to **(2)** before a final phase change to the monohydrated CAF.³ The lattice energies of the polymorphs were calculated by two methods. The first method, PIXEL developed by Gavezzotti,

and secondly by CrystalExplorer (CE) developed by Turner *et al.*^{31, 51} The PIXEL method functions by calculating a theoretical EDD for the asymmetric unit molecules individually using Gaussian09, then calculates the lattice energy by summation of pixelated partitioned space using symmetry operators.⁴⁹ Turner's CE method works by summation of the pairwise interaction energies between molecules generated from a dispersion and Density Functional Theory (DFT) wavefunction.³¹ PIXEL and CE calculations were performed at the MP2/6-31+G(d,p) level of theory, with an additional CE set calculated at B3LYP/6-31+G(d,p), as a comparison. Lattice energy values are shown in Table 5.

Table 5. Lattice energies, Dipole moments, and calculated in-crystal entropy for (1) and (2).^{31,51,52,53}

	Method	Functional and Basis Set	Lattice Energy (kJ·mol ⁻¹)	Molecular Dipole Moment (EXP) (D)	Entropy (J·K ⁻¹ ·mol ⁻¹)
(1)	PIXEL	MP2/6-31G(d,p)	-155.00	7.45	123.26
(2)	PIXEL	MP2/6-31G(d,p)	-158.90	4.93	112.88
(1)	CE	MP2/6-31G(d,p)	-101.13	-	-
(2)	CE	MP2/6-31G(d,p)	-107.14	-	-

(1)	CE	B3LYP/6- 31G(d,p)	-132.74	-	-
(2)	CE	B3LYP/6- 31G(d,p)	-134.05	-	-
(1)	CE	B3LYP/6- 31G(d,p) pair- wise corrected	-135.85	-	-
(2)	CE	B3LYP/6- 31G(d,p) pair- wise corrected	-133.36	-	-

The MP2 lattice energies agree with Thakuria *et al.* findings with a modestly increased stability throughout the series for (2).³ However, the B3LYP (a lower level of accuracy) models paint a mixed picture, contrary to the observed trend. Thomas *et al.* highlighted the difficulty in lattice energy calculations in polymorphic systems, and this was further expanded when studying 5-methyl-2-[(2-nitrophenyl)amino]-3-thiophenecarbonitrile generally referred to as ROY, noting that the B3LYP CE method was unreliable for the determination of lattice energies in conformational polymorphs, but the MP2 method offers better outcomes.^{36,54} Noting the above the remainder of the section will be referring to lattice energies obtained by the MP2 method. As expected, both approaches found the stabilities within ± 6 kJ mol⁻¹ for the polymorphs. This was expected considering the previous finding for other conformational polymorphs. An example being α -glycine, where lattice energies for each polymorph falling within experimental error of ± 10 kJ mol⁻¹.³⁰ As such, the near equivalent lattice

energies suggest that solvation by incoming water in humidity testing was critical in the change in physical stability, whereby the polar solvents ability to interact with hydrogen bond donors or acceptors is the discriminating factor that separates these conformational polymorphs. The molecular dipole moment (MDM) representative of the charge separation across a molecule offers a way to review how a crystal system responds to polar solvents. The MDM is enhanced in a crystalline state due to the intermolecular bonding and crystal field effects. The MDM of **(1)** is larger than that of **(2)** by 2.5D, (7.45 vs. 4.93, respectively), indicating that under the present of a polar solvent, **(1)** will react more rapidly. These findings correlate with the physical solvation stability seen experimentally. This situation is possibly due to the lower percentage of hydrogen contacts involved in **(1)**, allowing for an environment more volatile to hydrogen bonding than **(2)**. The MDM of **(2)** suggests that a polar solvent will still interfere with the crystal interface. However, it would be expected to be slower than that of **(1)** once again following the observed trend.

Another method for predicting solvation stability is to examine the in-crystal motion of molecules as a function of temperature; this is commonly referred to as solid-state entropy ($\Delta S_{\text{vib}}(T)$). A higher $\Delta S_{\text{vib}}(T)$ implies a greater potential to be soluble, resulting in a more negative Gibbs Free energy of solvation (ΔG_{sol}), indicating that crystals hydration to be a more spontaneous process. Madsen *et al.* developed a method for the calculation of entropy represented in Equation 4:

Equation 4.

$$\langle u^2 \rangle = \frac{h}{8\pi^2 \mu \nu} \coth\left(\frac{h\nu}{2kT}\right) \quad (4)$$

and Equation 5.

$$S_{\text{vib}}(T) = nR \left(\frac{h\nu}{kT} \left[\exp\left(\frac{h\nu}{kT}\right) - 1 \right]^{-1} \right) - \ln \left[1 - \exp\left(-\frac{h\nu}{kT}\right) \right] \quad (5)$$

The entropy calculation was performed at 298K to reflect the typical hydration environment. To analyse the in-crystal entropy, the atomic motion of each molecule is described by the TLS (translation, libration, screw) model.⁵² Whereby, the correlation between the translation and

libration modes of a molecule are defined as rigid bodies and describe vibration, as represented by $\langle u^2 \rangle$, h is Planck's constant, k is Boltzmann's constant. Assuming that a simple-harmonic model can be applied to the vibrations of T and L's $\langle u^2 \rangle$, the normal mode vibrational frequencies (ν) can be calculated using Equation 4, and ν is denoted as wavenumbers.^{52,53,55,56} The normal modes were calculated of the experimental data for (1) and (2) using the THMA11 program for thermal motion analysis.⁵⁶ Using these frequencies (ν) derived from Equation 4, the vibrational entropy of the crystal can be calculated as function of temperature as described in Equation 5. The resultant values of these calculations can be seen in Table 5, (1) has a higher entropy than that of (2), suggesting that solvation/hydration of the crystal would occur more readily and more spontaneously, once again, in agreement with experimental findings.³ Similarly, it indicates that the hydration of (2) is a less spontaneous event reflecting the extended hydration timeline described by Thakuria *et al.*²

In summary, it appears that the crystalline lattice stability of (1) and (2) are near equivocal, suggesting the hydration stability seen in (2) is a result of how it reacts to the incoming water. The MDM and in-crystal entropy highlight it as more resilient to hydration than that of (1).

CONCLUSION

A theoretical and experimental EDD study of both CAF-GLU form I, (1), and form II, (2), respectively, were performed to examine and rationalise at the electronic level the observations of Thakuria *et al.*³ The study showed that both forms were geometrically similar corresponding with previous studies.^{2,3} However, the topology highlighted the conformational dimorphs had a minimal difference in internal EDD. However, the topological review found (2) was the only polymorph with an aromatic hydrogen cyclic system, providing further stability to this form. Hirshfeld analysis accompanied by fingerprint plot analysis showed that the hydrogen atoms were more occupied in contacts maintaining stronger van der Waals arrangements in (2) compared to (1), suggesting less weak interactions need to be outcompeted in (1) aligning with the rapid conversion to (2) seen in the humidity studies. The lattice energies of both forms were equivocal, as expected based on

Thomas *et al.* findings regarding ROY and oxalic acid, as such MDM and in-crystal entropy provided insight into the physically seen stability differences. The MDM and in-crystal entropy of (1) are 7.45D and $123.26 \text{ J}\cdot\text{K}^{-1}\cdot\text{mol}^{-1}$, respectively, these values are larger than what was calculated for (2), 4.93D and $112.88 \text{ J}\cdot\text{K}^{-1}\cdot\text{mol}^{-1}$, respectively, suggesting that (1) is more likely to interact with a polar solvent such as water and will rapidly convert to (2). However, the hydration of (2) will still occur but at a slower rate. It is certain that (2) is the more stable dimorph in humid conditions corresponding to the experimental observations, and (1) is correctly coined a metastable dimorph of the co-crystals. Further work is required to evaluate which dimorph will have better pharmacokinetic profiling. Physical testing, such as dissolution testing, should be considered in the future to determine the more applicable co-crystal for the market formally.

ASSOCIATED CONTENT

Supporting Information

Data collection, treatment and refinement methods, residual density analysis, crystallographic data, topological findings, Atomic charges can be found in ESI. The CIF data for (1) and (2) is all included. This material is available free of charge via the Internet at <http://pubs.acs.org>.

ASSOCIATED CONTENT

■ AUTHOR INFORMATION

Corresponding Author

*E-mail: david.hibbs@sydney.edu.au.

ORCID 

Paul W. Groundwater: 0000-0002-4932-2030

David E. Hibbs: 0000-0002-2635-2990

Notes

The authors declare no competing financial interest.

■ ACKNOWLEDGMENTS

The authors would like to acknowledge the Eora Nation's Gadigal people as Traditional Custodians of the land upon which this research was conducted. The authors would like to

pay their respect to elders both past, present and future; and we ask that all people gently walk, work, research and live on this land.

B.A.H, S.A.S, and F.L would like to thank The University of Sydney for scholarships.

REFERENCES

1. Brittain, H. G. Polymorphism in pharmaceutical solids, CRC Press **2016**.
2. Thakuria, R.; Arhangelskis, M.; Eddleston, M. D.; Chow, E. H.; Sarmah, K. K.; Aldous, B. J.; Krzyzaniak, J. F.; Jones, W. Cocrystal Dissociation under Controlled Humidity: A Case Study of Caffeine–Glutaric Acid Cocrystal Polymorphs. *Org. Process. Res. Dev.* **2019**, *23*, 845-851.
3. Trask, A. V.; Motherwell, W. D. S.; Jones, W. Pharmaceutical Cocrystallization: Engineering a Remedy for Caffeine Hydration. *Cryst. Growth. Des.* **2005**, *5*, 1013-1021.
4. Reyes, C. M.; Cornelis, M. C. Caffeine in the Diet: Country-Level Consumption and Guidelines. *Nutrients*, **2018**, *10*, 1772.
5. Mishra, M. K.; Mishra, K.; Narayan, A.; Reddy, C. M.; Vangala, V. R. Structural Basis for Mechanical Anisotropy in Polymorphs of a Caffeine–Glutaric Acid Cocrystal. *Cryst. Growth. Des.* **2020**, *20*, 6306-6315.
6. Chow, P. S.; Lau, G.; Ng, W. K.; Vangala, V. R. Stability of Pharmaceutical Cocrystal During Milling: A Case Study of 1:1 Caffeine–Glutaric Acid. *Cryst. Growth. Des.* **2017**, *17*, 4064-4071.
7. Lai, F.; Du, J. J.; Williams, P. A.; Váradi, L.; Baker, D.; Groundwater, P. W.; Overgaard, J.; Platts, J. A.; Hibbs, D. E. A comparison of the experimental and theoretical charge density distributions in two polymorphic modifications of piroxicam. *Phys. Chem. Chem. Phys.* **2016**, *18*, 28802-28818.
8. Overgaard, J.; Hibbs, D. E. The Experimental Electron Density in Polymorphs A and B of the Anti-ulcer Drug Famotidine. *Acta. Crystallogr. A.* **2004**, *60*, 480-487.
9. Hawkins, B. A.; Du, J. J.; Lai, F.; Williams, P. A.; Groundwater, P. W.; Platts, J. A.; Overgaard, J.; Hibbs, D. E. *IN PRESS* **2020**.
10. Kulkarni, G. U.; Kumaradhas, P.; Rao, C. N. R. Charge Density Study of the Polymorphs of p-Nitrophenol. *Chem. Mater.* **1998**, *11*, 34998-3505.
11. Hoser, A. A.; Jarzemska, K. N.; Dobrzycki, Ł.; Gutmann, M. J.; Woźniak, K. Differences in Charge Density Distribution and Stability of Two Polymorphs of Benzidine Dihydrochloride. *Cryst. Growth. Dev.* **2012**, *12*, 3526-3539.

12. Schmidtman, M.; Farrugia, L. J.; Middlemiss, D. S.; Gutmann, M. J.; McIntyre, G. J.; Wilson, C. C. Experimental and Theoretical Charge Density Study of Polymorphic Isonicotinamide–Oxalic Acid Molecular Complexes with Strong O···H···N Hydrogen Bonds. *J. Chem. Phys. A*, **2009**, *113*, 13985-13997.
13. Dubey, R.; Pavan, M. S.; Guru Row, T. N.; Desiraju, G. R.; Crystal landscape in the orcinol:4,4'-bipyridine system: synthon modularity, polymorphism and transferability of multipole charge density parameters. *IUCrJ*, **2014**, *1*, 8-18.
14. Hathwar, V. R.; Thakur, T. S.; Dubey, R.; Pavan, M. S.; Guru Row, T. N.; Desiraju, G. R.; Extending the Supramolecular Synthon Based Fragment Approach (SBFA) for Transferability of Multipole Charge Density Parameters to Monofluorobenzoic Acids and their Cocrystals with Isonicotinamide: Importance of C–H···O, C–H···F, and F···F Intermolecular Regions. *J. Chem. Phys. A*, **2011**, *115*, 12852-12863.
15. Pavan, M. S.; Sarkar, S.; Row, T. N. G., Exploring the rare S–H...S hydrogen bond using charge density analysis in isomers of mercaptobenzoic acid. *Acta. Crystallogr. B.*, **2017**, *73*, 626-633.
16. Munshi, P.; Jelsch, C.; Hathwar, V. R.; Guru Row, T. N. Experimental and Theoretical Charge Density Analysis of Polymorphic Structures: The Case of Coumarin 314 Dye. *Cryst. Growth. Dev.* **2010**, *10*, 1516-1526.
17. Sovago, I.; Gutmann, M. J.; Senn, H. M.; Thomas, L. H.; Wilson, C. C.; Farrugia, L. J. Electron density, disorder and polymorphism: high-resolution diffraction studies of the highly polymorphic neuralgic drug carbamazepine. *Acta. Crystallogr. B.*, **2016**, *72*, 39-50.
18. Bader, R. F. W. *Atoms in Molecules: A Quantum Theory*, Oxford Univ. Press, 1994.
19. Frisch, M.; Trucks, G.; Schlegel, H. B.; Scuseria, G.; Robb, M.; Cheeseman, J.; Scalmani, G.; Barone, V.; Mennucci, B.; Petersson, G. *et al. Gaussian Inc., Wallingford, CT* **2009**, 200.
20. Becke, A. D. A new mixing of Hartree–Fock and local density-functional theories. *J. Chem. Phys.* **1993**, *98*, 1372-1377.
21. Lee, C.; Yang, W.; Parr, R. G. Development of the Colle-Salvetti correlation-energy formula into a functional of the electron density. *Phys. Rev. B.* **1988**, *37*, 785-789.
22. Tawada, Y.; Tsuneda, T.; Yanagisawa, S.; Yanai, T.; Hirao, K. A long-range-corrected time-dependent density functional theory. *J. Chem. Phys.* **2004**, *120*, 8425-8433.
23. Volkov, A.; Macchi, P.; L. Farrugia, J.; Gatti, C.; Mallinson, P.; Richter, T.; Koritsanszky, T.; XD-2006: A Computer Program Package for Multipole Refinement, Topological Analysis of Charge Densities and Evaluation of Intermolecular Energies from Experimental or Theoretical Structure Factors. *State University of New York, Buffalo, New York, USA.* **2006**.

24. Keith, T. A. AIMAll. *Overland Park KS, USA*. **2014**.
25. Leiserowitz, L. *Acta. Molecular Packing Modes. Carboxylic acids. Crystallogr. B*. **1976**, 32, 775-802.
26. Farrugia, L. J. ORTEP-3 for Windows - a version of ORTEP-III with a Graphical User Interface (GUI). *J. Appl. Crystallogr.*, **1997**, 30, 565.
27. Macrae, C. F.; Sovago, I.; Cottrell, S. J.; Galek, P. T. A.; McCabe, P.; Pidcock, E.; Platings, M.; Shields, G. P.; Stevens, J. S.; Towler, M.; Wood, P. A. Mercury 4.0: from visualisation to analysis, design and prediction. *J. Appl. Crystallogr.* **2020**, 53, 226-235
28. Spek, A. PLATON, An Integrated Tool for the Analysis of the Results of a Single Crystal Structure Determination. *Acta. Crystallogr. A*. **1990**, 46, c34-c34.
29. Turner, M. J.; McKinnon, J. J.; Jayatilaka, D.; Spackman, M. A. Visualisation and characterisation of voids in crystalline materials. *CrystEngComm* **2011**, 13, 1804-1813.
30. Berkovitch-Yellin, Z.; Leiserowitz, L. The Role Played by C-H...O and C-H...N Interactions in Determining Molecular Packing and Conformation. *Acta. Crystallogr. B*. **1984**, 40, 159-165.
31. Turner, M.; McKinnon, J.; Wolff, S.; Grimwood, D.; Spackman, P.; Jayatilaka, D.; Spackman, M. CrystalExplorer17. University of Western Australia **2017**.
32. Coppens P. X-Ray Charge Densities and Chemical Bonding, Oxford Univ. Press New York, **1997**.
33. Bernstein, J.; Etter, M. C.; Leiserowitz, L.; Hans-Beat, B. Dunitz, J. D. The Role of Hydrogen Bonding in Molecular Assemblies. *Structure Correlation* **1994**, 431-507.
34. Waller, M. P.; Robertazzi, A.; Platts, J. A.; Hibbs, D. E.; Williams, P. A. Hybrid density functional theory for π -stacking interactions: Application to benzenes, pyridines, and DNA bases. *J. Comput. Chem.* **2006**, 27, 491-504.
35. Gavezzotti, A.; Filippini, G. Geometry of the Intermolecular X-H. (X, Y = N, O) Hydrogen Bond and the Calibration of Empirical Hydrogen-Bond Potentials. *J. Chem. Phys.* **1994**, 98, 4831-4837.
36. Thomas, S. P.; Spackman, P. R.; Jayatilaka, D.; Spackman, M. A. Accurate Lattice Energies for Molecular Crystals from Experimental Crystal Structures. *J. Chem. Theory. Comput.* **2018**, 14, 1614-1623.
37. Espinosa, E.; Souhassou, M.; Lachekar, H.; Lecomte, C. *Acta Cryst.B*, **1999**, B55, 563-572.
38. Koch, U.; Popelier, P. L. A. Characterization of C-H-O Hydrogen Bonds on the Basis of the Charge Density. *J. Phys. Chem.* **1995**, 99, 9747-9754.

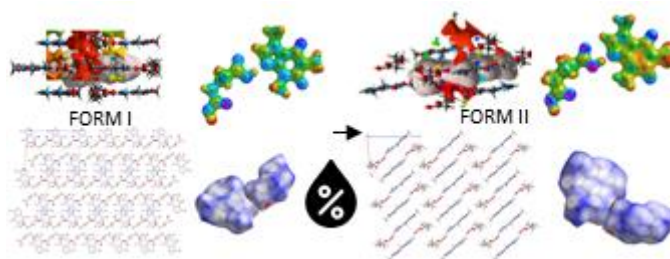
39. Ranganathan, A.; Kulkarni, G.U.; Rao, C. N.R. Probing the hydrogen bond through experimental charge densities. *J. Mol. Struct.* **2003**, 656, 249-263.
40. Wood, P. A.; Allen, F. H.; Pidcock, E. Hydrogen-bond directionality at the donor H atom—analysis of interaction energies and database statistics. *CrystEngComm*, **2009**, 11, 1563-1571.
41. Espinosa, E.; Souhassou, M.; Lachekar, H.; Lecomte, C. Topological analysis of the electron density in hydrogen bonds. *Acta. Crystallogr. B.* **1999**, 55, 563-572.
42. Espinosa, E.; Molins, E.; Lecomte, C. Hydrogen bond strengths revealed by topological analyses of experimentally observed electron densities. *Chem. Phys. Lett.* **1998**, 285, 170-173.
43. Abramov, Y. A. On the Possibility of Kinetic Energy Density Evaluation from the Experimental Electron-Density Distribution. *Acta. Crystallogr. A.* **1997**, A53, 264-272.
44. Hibbert, F.; Emsley, Hydrogen Bonding and Chemical Reactivity. *J. Adv. Phys. Org. Chem.* **1990**, 26, 255-379.
45. Nguyen, T. H.; Groundwater, P. W.; Platts, J. A.; Hibbs, D. E. Experimental and theoretical charge density studies of 8-hydroxyquinoline cocrystallised with salicylic acid. *J. Phys. Chem. A* **2012**, 116, 3420-3427.
46. Munshi, P.; Guru Row, T.N. Exploring the Lower Limit in Hydrogen Bonds: Analysis of Weak C–H···O and C–H··· π Interactions in Substituted Coumarins from Charge Density Analysis. *J. Phys. Chem. A.* **2005**, 109 (4), 659-672.
47. Nguyen, T. H.; Hibbs, D. E.; Howard, S. T. Conformations, energies, and intramolecular hydrogen bonds in dicarboxylic acids: implications for the design of synthetic dicarboxylic acid receptors. *J. Comput. Chem.* **2005**, 12, 1233-1241.
48. Jelsch, C.; Ejsmont, K.; Huder, L. The enrichment ratio of atomic contacts in crystals, an indicator derived from the Hirshfeld surface analysis. *IUCrJ*, 1(Pt 2), **(014)**. 119–128.
49. Du, J. J.; Váradi, L.; Williams, P. A.; Groundwater, P. W.; Overgaard, J.; Platts, J. A.; Hibbs, D. E. An analysis of the experimental and theoretical charge density distributions of the piroxicam–saccharin co-crystal and its constituents. *RSC. Adv.* **2016**, 6, 81578-81590.
50. Hübschle, C. B.; Dittrich, B. MoleCoolQt – a molecule viewer for charge-density research. *J. Appl. Crystallogr.* **2011**, 44, 238-240.
51. Gavezzotti, A. Calculation of lattice energies of organic crystals: the PIXEL integration method in comparison with more traditional methods. *Krist-Cryst. Mater.* **2005**, 220, 499-510.
52. Schomaker, V.; Trueblood, K. N. On the rigid-body motion of molecules in crystals *Acta. Crystallogr. B.* **1968**, 24, 63-76.

53. Madsen, A. Ø.; Larsen, S. Insight into Solid-State Entropy from Diffraction Data. *Angew. Chem. Int. Edit.* **2007**, 46, 8609-8613.
54. Thomas, S. P.; Spackman, M. A. The Polymorphs of ROY: A Computational Study of Lattice Energies and Conformational Energy Differences. *Aust. J. Chem.* **2018**, 71, 279-284.
55. Dunitz, J.; White, D. Non-rigid-body thermal-motion analysis. *Acta. Crystallogr. A.* **1973**, 29, 93-94.
56. Trueblood, K. N.; Huber-Buser, E.; Maverick, E. F. THMA11 program for thermal motion analysis, University of California, Los Angeles, **1987**.

“For Table of Contents Use Only”

Analysing Hydration differences in Co-crystal Polymorphs: A High-Resolution X-Ray Investigation of Caffeine-Glutaric Acid Co-crystals

Bryson A. Hawkins, Jaeyeon Han, Jonathan J. Du, Felcia Lai, Stephen A. Stanton, Shravan S. Divakarla, Paul W. Groundwater, James A. Platts, and David E. Hibbs*



Synopsis

In this study, the polymorphic co-crystals of Caffeine (CAF), and glutaric acid (GLU) originally engineered by Trask undergo charge density analysis to rationale the observed variation in hygroscopicity seen between the two forms.